EEET ECOLOGICAL ENGINEERING & ENVIRONMENTAL TECHNOLOGY

Ecological Engineering & Environmental Technology, 2026, 27(12), 341–357
https://doi.org/10.12912/27197050/241532
ISSN 2719–7050, License CC-BY 4.0

Received: 2026.09.15
Accepted: 2026.10.20
Published: 2026.11.02

Optical footprint and background control for rice leaf assessment using a miniature multispectral reflectance sensor

Kuni Faizah[1,2], Wahyono Wahyono[3], Jaka Widada[4], Valensi Kautsar[5], Iman Rahman[1], Yuliyan Dwi Prabowo[1], Arief Ika Uktoro[2], Kuwat Triyana[1*]

[1] Department of Physics, Universitas Gadjah Mada, Sekip Utara, Bulaksumur, Yogyakarta 55281, Indonesia
[2] Department of Agricultural Engineering, Institut Pertanian Stiper Yogyakarta, Jalan Nangka II, Maguwoharjo, Sleman 55283, Indonesia
[3] Department of Computer Science and Electronics, Universitas Gadjah Mada, Sekip Utara, Bulaksumur, Yogyakarta 55281, Indonesia
[4] Department of Agricultural Microbiology, Universitas Gadjah Mada, Jalan Flora, Bulaksumur, Yogyakarta 55281, Indonesia
[5] Faculty of Agriculture, Institut Pertanian Stiper Yogyakarta, Jalan Nangka II, Maguwoharjo, Sleman 55283, Indonesia
* Corresponding author's e-mail: triyana@ugm.ac.id

ABSTRACT

Reliable estimation of rice leaf nitrogen, chlorophyll, and SPAD supports precision nutrient management and crop phenotyping. However, measurements of narrow leaves are susceptible to background interference when the sensor footprint exceeds the target area. This study compared black and white backgrounds on the same rice leaves under a wide measurement geometry in 2023 and descriptively evaluated SPAD prediction using a redesigned narrow-geometry housing on an independent sample set collected in 2026. Spectra were collected from IR64 rice leaves at four growth stages and paired with SPAD, Kjeldahl nitrogen (%N), chlorophyll a, chlorophyll b, and total chlorophyll measurements. Under wide geometry, an 110 mm sensor-to-leaf distance and ±20.5° field of view produced an approximately 82 mm footprint, exposing an estimated 68–85% of the measurement area to the background. The white background increased raw signals by up to 10–11-fold in the blue region. Using five-fold outer and three-fold inner nested cross-validation, paired full 18-channel analyses of 140 leaves yielded pooled OOF R^2 values for black versus white backgrounds of 0.620 versus 0.588 for SPAD, 0.262 versus 0.371 for %N, 0.619 versus 0.434 for chlorophyll a, 0.486 versus 0.267 for chlorophyll b, and 0.567 versus 0.399 for total chlorophyll. Paired bootstrap comparisons showed no clear background-dependent difference for SPAD or %N, whereas the black background consistently improved chlorophyll a, chlorophyll b, and total chlorophyll predictions, with 95% confidence intervals for paired differences in R^2, RMSE, MAE, and CCC excluding zero. Fold-local Random Forest selection retained 2–17 wavelengths across folds and targets but did not consistently outperform the full 18-channel scenario. Under narrow geometry, a 10 mm sensor-to-leaf distance produced a nominal 7.5 mm optical footprint within a 30 mm sample opening. Using the full 18-channel scenario, SPAD prediction reached R^2 = 0.665, RMSE = 2.720, MAE = 2.122, and CCC = 0.810. Overall, background exposure was associated with target-dependent differences in prediction performance under the wide geometry, while the numerical SPAD performance of the independent narrow-geometry dataset cannot establish a geometry effect.

Keywords: proximal sensing; miniature multispectral sensor; optical footprint; background interference; rice leaf; leaf nitrogen; chlorophyll.

INTRODUCTION

Rice (*Oryza sativa* L.) is a major staple crop for more than half of the global population. In irrigated lowland systems, rice productivity depends strongly on balanced and timely nutrient management, particularly nitrogen (N) fertilization. However, blanket fertilizer recommendations may not adequately account for crop demand, growth stage, or field variability, potentially resulting in low nitrogen use efficiency (NUE), increased production costs, and reactive N losses to the environment (Govindasamy et al., 2023). Recent field evidence indicates that optimizing N application rates can maintain rice productivity while reducing ammonia volatilization and associated environmental burdens (Bi et al., 2025). Site-specific nutrient management (SSNM) addresses this limitation by adjusting nutrient inputs according to crop requirement, fertilizer source, and field condition. A recent on-farm study in Indonesian lowland rice showed that SSNM using locally available compound NPK fertilizer and urea increased grain yield by 0.4 mg ha^{-1} and gross return above fertilizer cost by 173 USD ha^{-1} compared with farmers' fertilizer practice, while using less N and P and only slightly more K (Girsang et al., 2025). These findings emphasize the need for timely crop-status information to support more efficient and environmentally responsible nutrient management.

Leaf nitrogen concentration, chlorophyll content, and SPAD value are important indicators of rice nutritional status and photosynthetic capacity. These traits are closely associated with plant N uptake and have been used to support N diagnosis and fertilizer decision-making in rice (Wang et al., 2024). However, conventional laboratory methods, including Kjeldahl digestion and solvent-based chlorophyll extraction, are destructive, labor-intensive, and unsuitable for repeated in-season monitoring. Rapid, non-destructive optical sensing may contribute to estimating crop nitrogen status, including indices such as the Nitrogen Nutrition Index (NNI; Lizana et al., 2025). However, translating sensor-derived estimates into fertilizer decisions requires independent validation against nitrogen-sufficiency thresholds and observed crop responses.

The Konica Minolta SPAD-502 is widely used as a benchmark for non-destructive chlorophyll assessment and N fertilizer timing. This approach measures light transmittance through the leaf tissue at two specific wavelengths 650 nm (red) and 940 nm (near infrared), to calculate a relative index expressed in non-dimensional SPAD units. Unlike this leaf-clamped transmission measurement, the AS7265x configuration used here measures light reflected from the leaf. The silicon-based AS7265x multispectral triad provides 18 channels spanning 410–940 nm and has a nominal aperture-limited field of view of ±20.5° (SparkFun Electronics, 2023). Its three spatially separate sensor devices each have an optical aperture; consequently, the area sampled on the leaf depends on sensor-to-leaf distance and device alignment (OSRAM, 2018).

Under the wide-footprint geometry evaluated in the present study, the AS7265x was positioned 110 mm above the leaf surface. Combined with its nominal ±20.5° field of view, this distance produced a calculated optical footprint of approximately 82 mm in diameter. For rice leaves 10–20 mm wide, the exposed background was estimated to occupy approximately 69–85% of the measurement area. Background effects are also recognized in multispectral imaging, where soil, shadows, crop residues, and other nontarget surfaces can influence spectral information (Hale et al., 2023; Tian et al., 2024). However, imaging systems can partly address this problem through segmentation or masking because target and background pixels are spatially separated (Pei et al., 2025). In contrast, non-imaging point sensors such as the AS7265x record a single integrated signal from all surfaces within the field of view. Consequently, when the sensor footprint exceeds the leaf area, the resulting spectrum represents a mixture of leaf and background responses.

Previous work has reported spectral variability when the AS7265x measures narrow leaves and suggested that its separate sensor apertures may contribute to this variability (Lopin et al., 2025). However, how a change in the exposed background affects both the recorded signals and trait-prediction performance under a wide footprint remains insufficiently characterized. The present study addresses this gap by comparing black and white backgrounds on the same rice leaves. It also reports SPAD prediction using a redesigned, shorter-distance configuration on an independent sample set; this comparison is descriptive and cannot isolate the effect of footprint size.

Accordingly, this study evaluated two practical optical-control strategies for a miniature AS7265x multispectral reflectance sensor: (1) background

control using black and white surfaces under a wide measurement geometry and (2) optical-footprint control by reducing the sensor-to-leaf distance through housing redesign. Under the wide geometry, wavelength-dependent background effects and prediction performance were evaluated for SPAD, leaf nitrogen, chlorophyll a, chlorophyll b, and total chlorophyll using full- and selected-wavelength models. A complementary narrow-geometry experiment evaluated SPAD prediction using the redesigned housing with a shorter sensor-to-leaf distance.

MATERIALS AND METHODS

Rice leaf sampling and reflectance measurements

Rice leaves of the IR64 variety, an irrigated lowland rice type, were collected in Yogyakarta, Indonesia, during two independent sampling campaigns. For the wide-geometry experiment, leaves were collected in 2023 from four separate rice-field plots within the same sampling area, with one plot representing each growth stage: tillering, maximum tillering, panicle initiation, and maturity. The coordinates 7°44′52.0″ S and 110°25′18.4″ E indicate the approximate center of the sampling area rather than a single sampling point. For the narrow-geometry experiment, an independent set of IR64 leaves was collected from the same general sampling area in 2026 to evaluate the redesigned housing.

The 2023 wide-geometry experiment included 141 biological leaf samples. White-background measurements were available for 141 leaves across tillering (n = 30), maximum tillering (n = 40), panicle initiation (n = 25), and maturity (n = 46). Black-background measurements were available for 140 of the same leaves, with stage counts of 30, 40, 24, and 46, respectively, yielding 140 complete black–white pairs. The 2026 narrow-geometry experiment included 228 biological leaf samples across the same stages (n = 70, 49, 40, and 69, respectively). The experiments differed in sampling year and sample set and were analyzed independently. Leaf sampling and growth-stage identification were conducted by an agronomist specializing in rice physiology.

In both experiments, measurements were obtained from the fourth fully expanded leaf from the top. Each leaf was assigned a unique biological-sample ID, which was retained on its SPAD record, spectral measurements, and, where applicable, labelled laboratory samples. At the field site, three SPAD readings were taken at the two-thirds position of each leaf (Yuan et al., 2016) using Konica Minolta SPAD-502 chlorophyll meter. The readings were averaged to obtain one SPAD reference value per biological sample. The leaf was then excised and immediately placed in an opaque black container before spectral measurement.

SPAD and spectral measurements were performed consecutively within the same sampling session. In the 2023 wide-geometry experiment, spectral readings were acquired first with the black background and then with the white background. In both experiments, at least three spectral readings were acquired per leaf under each applicable measurement configuration. Following spectral acquisition, each 2023 leaf was divided into two portions: one for chlorophyll extraction and the other placed in a labelled bag for drying and nitrogen analysis. The corresponding biological-sample ID was used to match each leaf's SPAD value, spectral profile, and laboratory reference values. SPAD was the reference trait measured in the 2026 narrow-geometry experiment; nitrogen and chlorophyll reference measurements were obtained for the 2023 wide-geometry experiment only.

Leaf nitrogen concentration (%N) was determined by the semi-micro Kjeldahl method (Sáez-Plaza et al., 2013). Leaf samples were oven-dried at 80 °C for 24 h and ground. A 0.2 g portion of dried tissue was digested with concentrated H_2SO_4 and a selenium catalyst until a clear digest was obtained. Following alkalinization with NaOH, the released ammonia was distilled into boric acid and titrated with standard H_2SO_4. Nitrogen concentration was expressed as a percentage of dry weight.

Chlorophyll a (Chl a), chlorophyll b (Chl b), and total chlorophyll (Total Chl) were determined from the fresh leaf portion using Arnon's spectrophotometric method (Arnon, 1949). After removal of the midrib, approximately 0.1 g of fresh leaf tissue was weighed individually for each sample and extracted with 80% acetone to a final volume of 20 mL. Absorbance at 663 and 645 nm was measured three times per sample, and the readings were averaged. Chlorophyll concentrations were calculated using the recorded fresh mass of each sample and expressed as mg g^{-1} fresh weight (Lichtenthaler & Buschmann, 2001).

Sensing system and optical configuration

Spectral data were obtained using a portable non-imaging multispectral sensing system based on the AS7265x sensor (SparkFun Electronics, Niwot, CO, USA), which provides 18 spectral channels across 410–940 nm. Measurements were acquired using an integration time of 140 ms and a gain setting of 64×. Before measurements, it was powered on and allowed to warm up for at least 10 min. The light-shielded housing maintained the specified sensor-to-leaf distance and reduced exposure to ambient light.

A dark-reference measurement was first acquired with the onboard LEDs switched off and the housing closed. No signal was recorded across the spectral channels under these conditions. A Spectralon® 99% diffuse reflectance standard was then measured with the sensor illumination active to provide the white reference. Spectralon was measured periodically during leaf acquisition in each sampling period (2023 and 2026). For leaf measurements, the onboard white, ultraviolet, and infrared LEDs were activated. Spectral readings were acquired per leaf under each applicable measurement configuration. In the 2023 wide-geometry experiment, readings with the black background preceded those with the white background. Normalized reflectance at each output wavelength was calculated using white- and dark-reference correction (Yang et al., 2020).

$$R = \left(\frac{I_{sample} - I_{dark}}{I_{spectralon} - I_{dark}}\right) \times 0.99 \quad (1)$$

where: I_{sample}, $I_{spectralon}$, and I_{dark} represent the raw intensities of the leaf sample, Spectralon® reference.

Because the recorded dark-reference values were zero across the spectral channels in this study, the dark-reference terms did not change the calculated reflectance. At the repeat level, normalized channel values were checked before sample-level averaging. A reading was excluded if any of its 18 normalized channels exceeded 1.0. Eight white-background readings were excluded on this basis; none were excluded from the black-background or narrow-geometry datasets, and no biological sample was lost (Table S1). The retained raw readings were averaged within each biological sample and measurement configuration, and the mean raw spectrum was normalized using the Spectralon and dark references to obtain one reflectance profile per sample and configuration.

For the wide-geometry experiment, the sensor was mounted in a fixed light-shielded black housing with an approximately 110 mm sensor-to-sample distance. The optical sampling footprint was defined by the AS7265x field of view (FoV; ±20.5°, equivalent to a 41° full cone angle), the footprint diameter (d) was estimated as $d = 2\,h\,\tan(20.5°)$. For centrally positioned leaves 10 and 20 mm wide, the estimated fractions of the circular footprint occupied by exposed background were approximately 84.6% and 69.4%, respectively. These values describe geometric area, not the measured contribution of background-reflected energy. For the narrow-geometry experiment, the redesigned housing incorporated an approximately 30 mm circular sample opening and reduced the sensor-to-leaf distance to 10 mm, yielding a nominal footprint diameter of approximately 7.5 mm per sensor device (Fig. 1). Because the narrow-geometry experiment used an independent sample set collected in a different year, comparisons of predictive performance between the two geometries were descriptive.

To evaluate background interference experimentally, black and white office paper were used as controlled backgrounds during reflectance acquisition. The black background showed L* = 36.27 ± 0.19, a* = 0.20 ± 0.06, and b* = 5.56 ± 0.05, whereas the white background showed L* = 95.77 ± 0.84, a* = 1.04 ± 0.13, and b* = 2.89 ± 0.13. Their mean lightness value differed by 59.50 L* units.

Machine learning modelling, feature selection, and agreement analysis

Machine learning models were developed using normalized AS7265x reflectance data for regression tasks. Regression models, including linear regression, ridge, lasso, support vector regression (SVR), k-nearest neighbors regression (k-NN), random forest (RF), and gradient boosting (GB), were used to predict SPAD, %N, chlorophyll a, chlorophyll b, and total chlorophyll.

All complete biological samples were evaluated using stratified nested cross-validation, comprising a five-fold outer loop and a three-fold inner loop. In each outer fold, approximately 80% of the samples were assigned to outer training and 20% to held-out outer validation. Within the outer-training data, two parallel modelling scenarios were evaluated: the full 18-wavelength set and RF-selected wavelength subsets. All

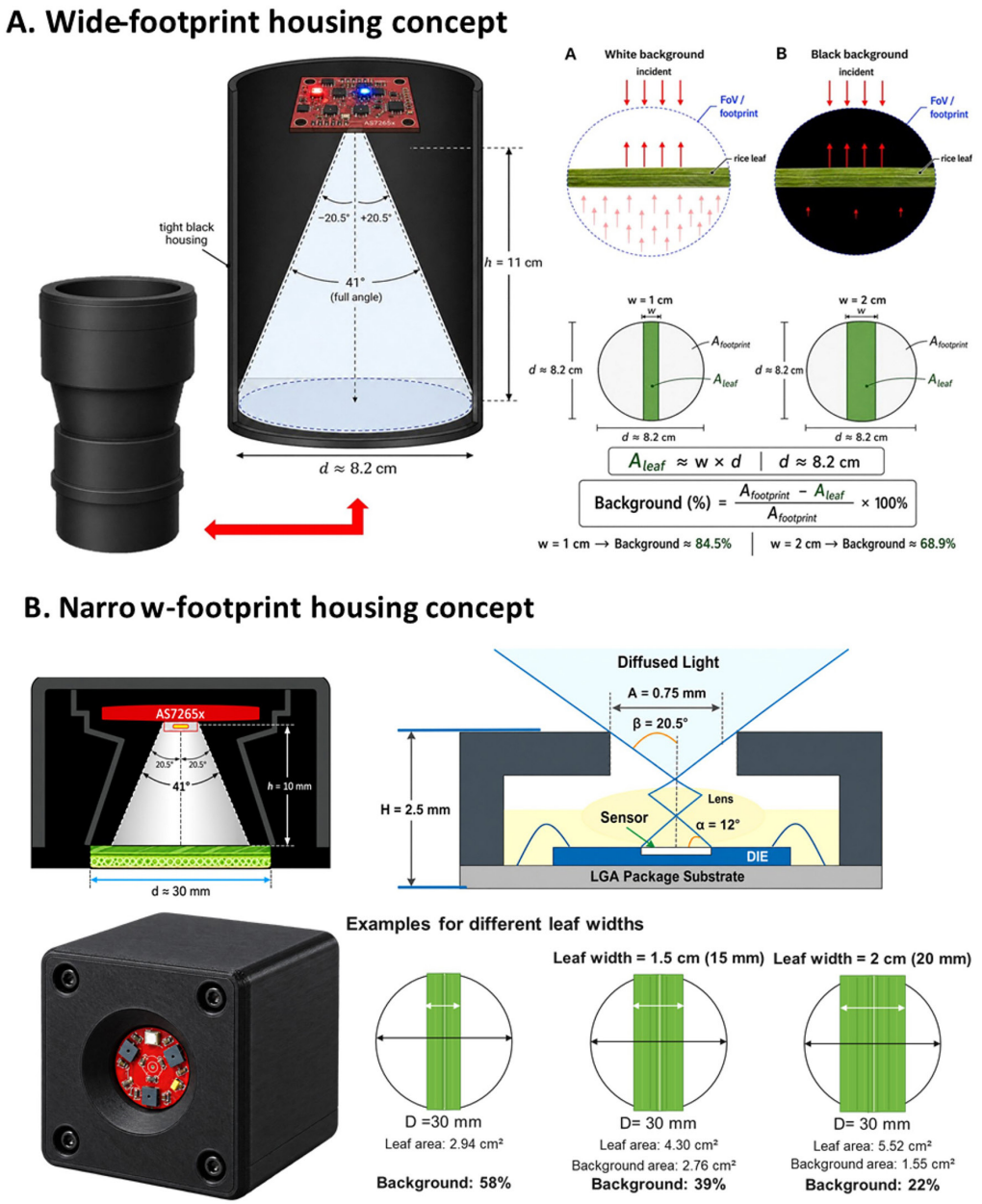

Figure 1. Schematic diagram of the AS7265x measurement setup and estimated background contribution under background and geometry configuration

preprocessing, Random Forest-based wavelength ranking, progressive subset selection, model fitting, and hyperparameter tuning were performed exclusively within the inner cross-validation loop to prevent data leakage. GridSearchCV was used for the full-wavelength scenario, whereas RandomizedSearchCV jointly optimized the wavelength selector and regression-model hyperparameters in the selected-wavelength scenario. For each candidate pipeline model selection was based on the mean inner-cross-validation RMSE:

$$\mathrm{RMSE}_m = \frac{1}{J}\sum_{j=1}^{J} \mathrm{RMSE}_{m,j},\ J = 3 \qquad (2)$$

where: $\mathrm{RMSE}_{m,j}$ is the validation RMSE of candidate pipeline m in inner fold j.

The corresponding standard error was calculated as

$$SE = \frac{s_m}{\sqrt{J}} \qquad (3)$$

where: s_m is the standard deviation of the inner-fold RMSE values.

Candidate pipelines were selected using the one-standard-error rule, whereby the simplest pipeline satisfying

$$\overline{\mathrm{RMSE}}_{\mathrm{m}} \leq \overline{\mathrm{RMSE}}_{\mathrm{min}} + \mathrm{SE}_{\mathrm{min}} \qquad (4)$$

was retained, where $RMSE_{min}$ denotes the lowest mean inner-CV RMSE and SE_{min} is its associated standard error. The selected pipeline was then refitted using the complete outer-training subset and evaluated on the corresponding outer-validation subset.

After completion of all five outer folds, each biological sample had one prediction generated exclusively from the outer-validation fold in which that sample had not been used for model fitting. The nested out-of-fold prediction for sample was therefore defined as

$$\hat{y}_i^{\mathrm{OOF}} = f^*_{k(i)}(\mathbf{x}_i) \tag{5}$$

where: $\mathbf{x}_i$ represents the spectral input of sample (i), $k(i)$ denotes the outer fold in which sample i served as validation data, and $f^*_{k(i)}$ is the pipeline selected and refitted using only the corresponding outer-training data.

Predictions from all five outer folds were pooled to calculate the overall nested OOF performance. Predictive performance was quantified using the coefficient of determination (R^2)

$$R^2_{OOF} = 1 - \frac{\sum_{i=1}^{n}\left(y_i - \hat{y}_i^{OOF}\right)^2}{\sum_{i=1}^{n}(y_i - \bar{y})^2} \tag{6}$$

root mean square error (RMSE),

$$\mathrm{RMSE}_{OOF} = \sqrt{\frac{1}{n}\sum_{i=1}^{n}\left(y_i - \hat{y}_i^{OOF}\right)^2} \tag{7}$$

and mean absolute error (MAE),

$$\mathrm{MAE}_{OOF} = \frac{1}{n}\sum_{i=1}^{n}\left|y_i - \hat{y}_i^{OOF}\right| \tag{8}$$

where: y_i and $\hat{y}_i^{OOF}$ are the reference and nested OOF-predicted values for sample i, respectively, $\bar{y}$ is the mean reference value, and n is the total number of biological samples.

The complete nested cross-validation workflow is illustrated in Figure 2.

To express prediction error relative to the dispersion of the reference values, the ratio of performance to interquartile distance (RPIQ) was calculated from the pooled nested OOF predictions,

$$\mathrm{RPIQ}_{OOF} = \frac{Q_{0.75}(y) - Q_{0.25}(y)}{\sqrt{\frac{1}{n}\sum_{i=1}^{n}\left(y_i - \hat{y}_i^{OOF}\right)^2}} \tag{9}$$

where $Q_{0.75}(y)$ and $Q_{0.25}(y)$ are the 75th and 25th percentiles of the reference values, respectively. Higher RPIQ values indicate smaller prediction errors relative to the interquartile spread of the reference data. RPIQ was included as a scale-adjusted descriptor of prediction error (Bellon-Maurel et al., 2010).

Agreement between nested out-of-fold (OOF) predictions and reference measurements was evaluated using Lin's concordance correlation coefficient (CCC) (Lin, 1989):

$$\rho_c = \frac{2s_{OP}}{s_O^2 + s_P^2 + (\bar{O} - \bar{P})^2} = rC_b \tag{10}$$

$$C_b = \frac{2}{v + v^{-1} + u^2}, v = \frac{s_P}{s_o}, u = \frac{\bar{P} - \bar{O}}{\sqrt{s_P s_o}} \tag{11}$$

where O and P denote the reference (observed) and nested OOF-predicted values, respectively; $\bar{O}$ and $\bar{P}$ are their means; s_{OP} is their covariance; s_O^2 and s_P^2 are their variances; r is Pearson's correlation coefficient, representing precision; and C_b is the bias-correction factor, representing location and scale agreement. In Eq. (11), $v = s_P/s_O$ denotes the relative scale shift, and u denotes the standardized location shift. Perfect agreement is obtained when $r = 1$, $v = 1$, and $u = 0$, resulting in $C_b = 1$ and ρ_c. Values of ρ_c approaching 1 indicate closer agreement with the 1:1 line. The 95% confidence intervals were estimated using 2000 paired percentile-bootstrap resamples of the reference-prediction pairs (Carpenter & Bithell, 2000). Differences in pooled OOF R^2, RMSE, MAE, and CCC were calculated as RF Selected − Full 18 within each dataset and as white − black using the 140 shared biological IDs. Within each of 2000 paired bootstrap resamples of biological IDs, R^2, RMSE, MAE, and CCC were recalculated for both compared scenarios on the same sampled IDs, and the difference between scenarios was recorded. The 2.5th and 97.5th percentiles of these paired differences formed the 95% CI; intervals excluding zero were interpreted as evidence of a directional difference (Tables S8 and S9). Because the white-background dataset included one additional biological sample, its 141-sample OOF metrics in Table 1 may differ slightly from those calculated on the 140 matched samples for the paired comparison.

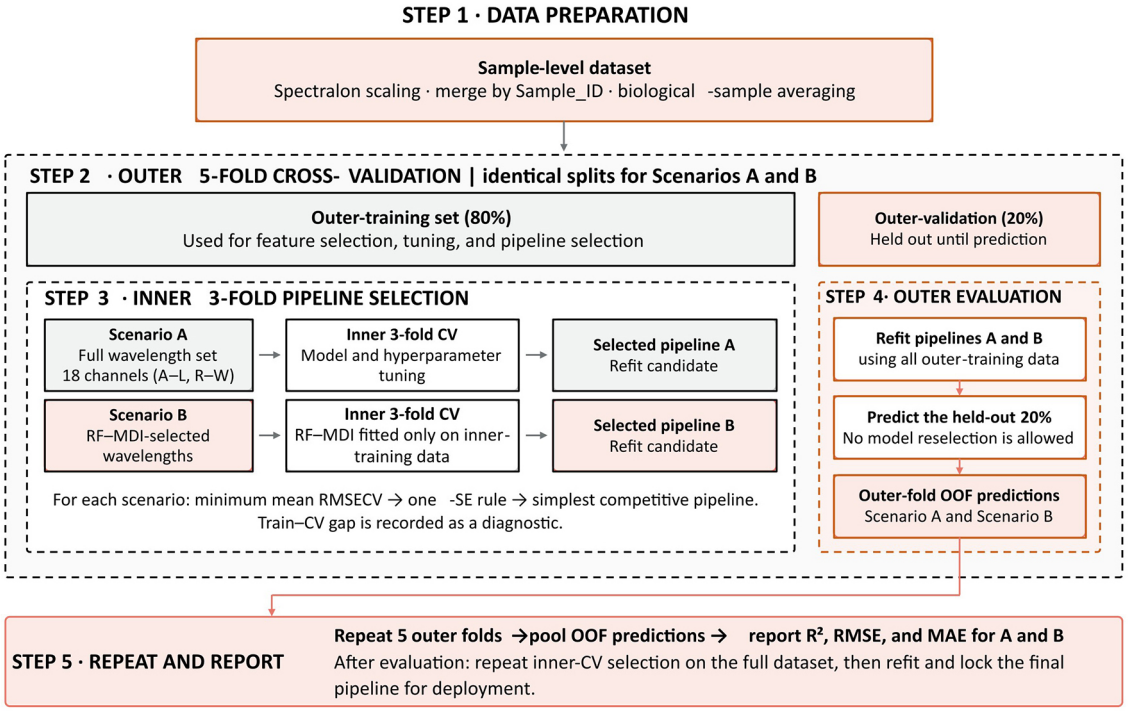

$\bar{O}-\bar{P}$

Figure 2. Nested cross-validation workflow used to compare Scenario A (the full 18-channel wavelength set) and Scenario B (RF–MDI-selected wavelengths). Feature selection, preprocessing, model tuning, and pipeline selection were performed within the inner three-fold cross-validation. The selected pipeline for each scenario was refitted on the complete outer-training set and evaluated on the held-out oute r-validation set. Predictions from the five outer folds were pooled to calculate out-of-fold R^2, RMSE, and MAE

Table 1. Model performance for predicting rice physiological traits using the full 18-channel input under black and white background configurations

Variable	Tillering	Max. tillering	Panicle init.	Mature	Range
SPAD – 2026 narrow (n = 228)	36.85 ± 4.23	37.05 ± 3.51	34.33 ± 3.41	30.01 ± 3.13	21.98–50.96
SPAD – 2023 wide (n = 140)	39.74 ± 1.49	36.88 ± 2.92	31.22 ± 3.27	28.20 ± 8.89	10.30–44.10
N (%) (n = 140)	2.55 ± 0.89	2.73 ± 0.56	2.26 ± 0.34	1.77 ± 0.38	0.69–4.24
Chl a (mg/g) (n = 140)	3.23 ± 0.48	4.24 ± 0.69	3.44 ± 1.09	1.78 ± 0.85	0.21–5.05
Chl b (mg/g) (n = 140)	1.69 ± 0.53	2.56 ± 0.67	2.16 ± 1.11	0.92 ± 0.45	0.14–4.23
Total Chl (mg/g) (n = 140)	4.92 ± 0.98	6.80 ± 1.18	5.60 ± 2.07	2.70 ± 1.27	0.35–9.15

RESULTS AND DISCUSSION

Physiological phenotypes of rice leaves across growth stages

Validation variables, including SPAD values, nitrogen content (%N), chlorophyll a (Chl a), chlorophyll b (Chl b), and total chlorophyll (Total Chl), showed substantial variation across the four sampled rice growth stages. According to previous studies, rice SPAD values generally fall within the range of 25–45 (Ghosh et al., 2020), although the IR64 variety has been reported to exhibit relatively lower SPAD values than some other genotypes, and SPAD values are typically higher during tillering and decline toward maturity (Vijayaraghavareddy et al., 2020).

Table 2 and Supplementary Figure S1 also show differences between the independently collected SPAD datasets. The 2026 narrow-geometry dataset (n = 228) spanned 21.98–50.96, whereas the 2023 wide-geometry dataset (n = 140) spanned 10.30–44.10. At maturity, SPAD variability was greater in the 2023 dataset (SD = 8.89) than in the 2026 dataset (SD = 3.13). Such differences are plausible between independent sampling campaigns, although their specific causes were not determined. Because differences in reference-value distributions

Table 2. Range of measured physiological phenotypes of rice leaves; SPAD, nitrogen (%N), and chlorophyll components (Chl a, Chl b, and total Chl), across four growth stages

Set-up	Prediction target	Best model (folds)	Inner-CV R^2	Nested OOF R^2 (95% CI)	OOF RMSE	OOF MAE	Best parameters
Black	SPAD	Lasso (3/5)	0.628 ± 0.048	0.620 (0.426–0.754)	4.432	3.154	α = 0.1–0.3
White	SPAD	LR (3/5)	0.552 ± 0.047	0.580 (0.426–0.684)	4.661	3.577	Default
Black	%N	KNN (3/5)	0.328 ± 0.049	0.262 (0.060–0.439)	0.593	0.41	k = 7–9; Manhattan; distance
White	%N	Lasso (3/5)	0.321 ± 0.042	0.371 (0.207–0.518)	0.545	0.394	α = 0.01–0.03
Black	Chl a	KNN (2/5)	0.612 ± 0.025	0.619 (0.496–0.711)	0.774	0.607	k = 3–5; Manhattan; distance
White	Chl a	LR (5/5)	0.400 ± 0.057	0.440 (0.248–0.576)	0.944	0.76	Default
Black	Chl b	KNN (4/5)	0.485 ± 0.048	0.486 (0.341–0.592)	0.677	0.535	k = 3–9; distance
White	Chl b	LR / ridge (2/5 each)	0.232 ± 0.061	0.265 (0.090–0.403)	0.824	0.648	Default / α = 1
Black	Total Chl	KNN (4/5)	0.583 ± 0.045	0.567 (0.425–0.671)	1.398	1.085	k = 3–7; distance
White	Total Chl	LR (4/5)	0.348 ± 0.054	0.408 (0.215–0.550)	1.652	1.325	Default

can affect model-performance metrics, the wide-versus-narrow SPAD comparison should be interpreted descriptively.

Nitrogen content in the present samples was also within biologically plausible ranges reported for rice leaves, including 0.52-3.69% under typical conditions (Miao et al., 2023) and up to 3.95-4.65% during active vegetative development (Xu et al., 2023). Likewise, chlorophyll-related variables remained within acceptable biological variation reported for rice (Liu et al., 2024; Mia et al., 2012; Weng et al., 2005). Nitrogen and chlorophyll reference values were measured only in the 2023 wide-geometry experiment and therefore cannot be compared between the two experiments. Taken together, these distributions indicate that the reference variables covered physiologically relevant ranges suitable for evaluating the sensing performance of the AS7265x system under the measurement conditions examined in this study.

Background contribution to mixed spectral signals in rice leaves

White-background measurements generated consistently higher raw spectral signals than black-background measurements across all rice growth stages (Fig. 3a-d), indicating that the AS7265x output was influenced by non-target surfaces within the sensor footprint. Therefore, the recorded signals represent background-affected sensor responses rather than true leaf reflectance. The white-to-black signal ratio was highest in the blue region, reaching approximately 10–11×, followed by the green region at 7.59–8.98×. Lower ratios were observed in the red, red-edge, and NIR regions, with values of approximately 4.23–4.66×, 5.01–5.74×, and 4.11–4.83×, respectively.

In true leaf reflectance, strong absorption in the blue and red regions results in low reflectance, while reflectance increases toward the red-edge and NIR regions as pigment absorption decreases. However, the AS7265x raw signal represents a mixed response from the leaf and exposed background within the sensor footprint. The higher signal measured with the white background is consistent with a greater contribution from the exposed surface within the sensor footprint. However, the separate leaf and background contributions were not quantified.

The red-edge region around 680–730 nm represents the transition from strong chlorophyll absorption in the red region to increased scattering in the near-infrared region. Because 680 nm is closely associated with chlorophyll absorption, changes in chlorophyll content can alter the slope toward the red-edge region, making this region a useful indicator of plant physiological status. However, in this study, the apparent red-edge pattern was also affected by background configuration. The transition appeared around 680v705–730 nm under the black background but shifted toward 705–730–760 nm under the white background.

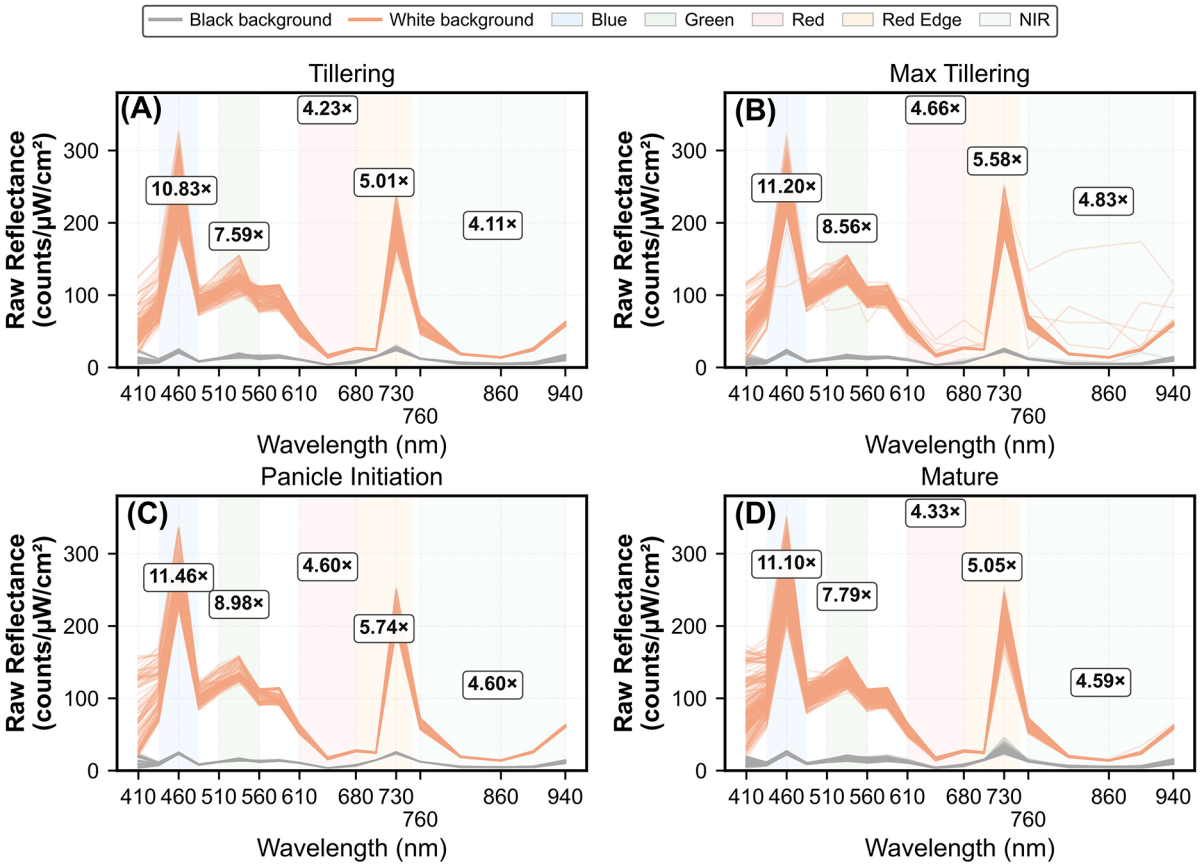

Figure 3. Effect of white and black background configurations on rice leaf raw reflectance spectra across four growth stages: tillering (a), maximum tillering (b), panicle initiation (c), and mature stage (d), with shaded spectral regions and average white-to-black signal ratios

Because the same leaf samples were measured under both configurations, this finding indicates that background interference can induce an apparent spectral shift in the recorded reflectance pattern.

Under the black-background configuration, the spectra showed a relatively weak NIR response and did not form the broad, stable high-reflectance plateau typically observed in leaf reflectance spectra (Fig. 4a-d). This pattern was comparable to that reported by Lopin et al. (2025) where the IR-region response was also reduced when the IR light source was not used. In contrast, the white-background configuration produced a higher but less stable long-wavelength response, which may partly reflect additional background contribution within the sensor footprint. Therefore, the NIR pattern observed in this study should be interpreted cautiously, as it may be influenced by illumination conditions and background effects rather than leaf reflectance alone.)

Effect of background configuration on model performance for predicting rice physiological traits

Model performance under black and white backgrounds is summarized in Table 2. Paired bootstrap comparisons on the 140 shared biological IDs supported higher full-channel OOF R^2 under black for Chl a, Chl b, and total chlorophyll. The SPAD and %N differences were inconclusive (Table S9). This pattern shows that the black-background measurements were associated with better predictive performance for chlorophyll a, chlorophyll b, and total chlorophyll; it does not identify which change in the measured signal accounts for that difference. This interpretation is consistent with observations in narrow rice leaves, where incomplete coverage of the optical path may introduce mixed contributions from the leaf and underlying background (Lopin et al., 2025).

With all 18 channels, pooled OOF R^2 under black versus white was 0.620 versus 0.580 for SPAD, 0.619 versus 0.440 for Chl a, 0.486 versus

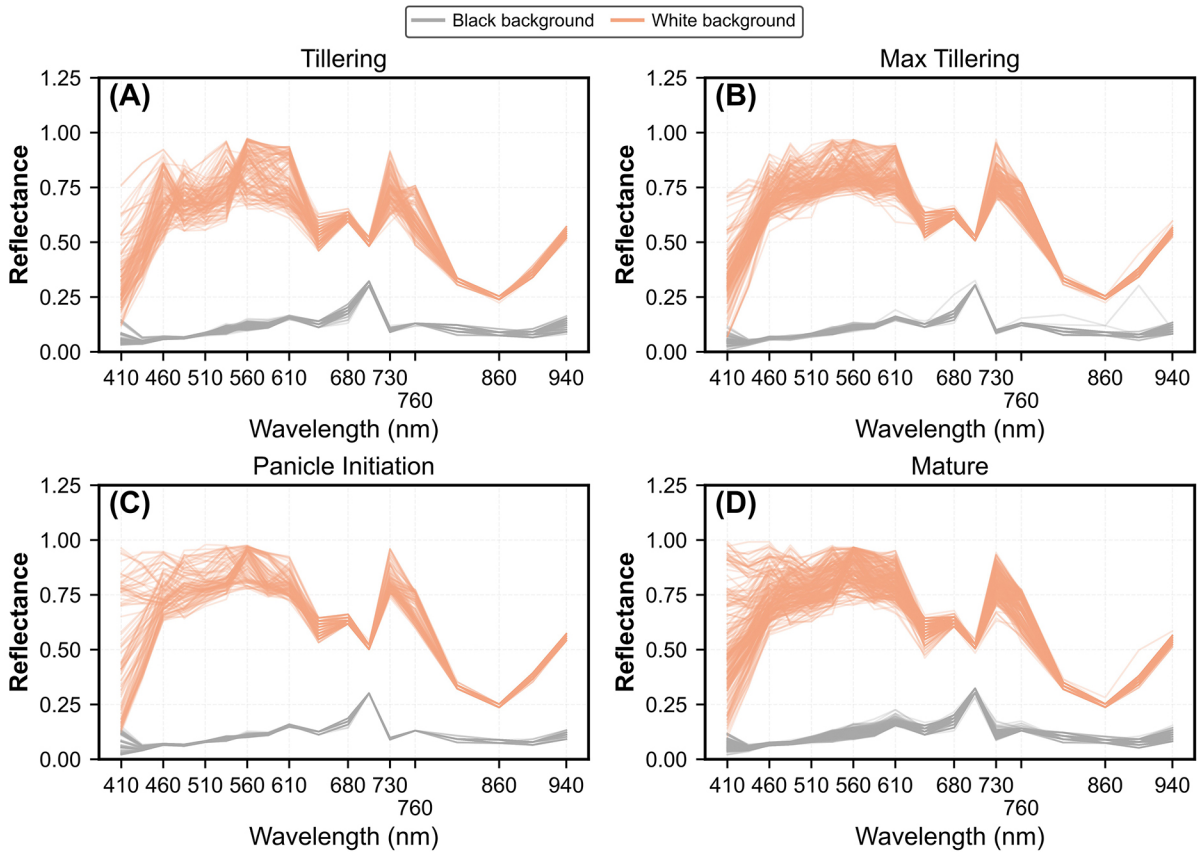

Figure 4. Reflectance spectra of rice leaves measured under white and black background configurations at four growth stages: tillering (a), maximum tillering (b), panicle initiation (c), and mature stage (d

0.265 for Chl b, and 0.567 versus 0.408 for total chlorophyll (Table 2). Paired white − black differences in R^2 were −0.186 (95% CI: −0.367 to −0.035), −0.219 (−0.377 to −0.074), and −0.168 (−0.326 to −0.022) for the three chlorophyll traits, respectively; the intervals for SPAD and %N included zero (Table S9). According to the background-interference energy-transfer framework, the recorded spectral energy comprises both leaf-reflected energy and background-derived energy. When the target does not fully occupy the sensor field of view, a highly reflective background can therefore increase the background component and distort the leaf spectral response (Chen et al., 2024). The higher signals measured with the white background are consistent with a greater background contribution. However, without a spectral-mixture or background-correction analysis, this study cannot determine whether background contribution, changes in leaf–background contrast or signal magnitude, or their combined effects primarily explain the difference in predictive performance.

Leaf nitrogen (%N) showed lower predictive performance than the chlorophyll-related traits. With all 18 channels, OOF R^2 was 0.262 under black and 0.371 under white. In the paired comparison, ΔR^2 (white − black) was 0.109 (95% CI: −0.045 to 0.256); the interval included zero. This result contrasts with Nogueira et al. (2025), who reported R^2 values of approximately 0.61–0.79 across maize growth stages and approximately 0.75 using multivariate PLSR with an AS7265x-based system. Their measurements were conducted on broader maize leaves, which may have provided more consistent target coverage within the sensor field of view and reduced the relative contribution of surrounding background. This comparison suggests that measurement configuration and target coverage may substantially influence the nitrogen-related information recoverable from AS7265x measurements (Nogueira et al., 2025).

Chlorophyll-related traits were predicted more successfully than leaf nitrogen, with OOF R^2 values of 0.619, 0.486, and 0.567 for Chl a, Chl b, and total chlorophyll, respectively, under the black background using all 18 channels. Their stronger

Table 3. Predictive performance of full-channel and selected-wavelength models under narrow and wide measurement geometries. Complete results are provided in Supplementary Tables S7–S9

Geometry	Scenario	Target	Best model (folds)	Inner-CV R^2	Nested OOF R^2 (95% CI)	OOF RMSE	OOF MAE	Best parameters
Narrow (n = 228)	Full 18	SPAD	LR (4/5)	0.641 ± 0.028	0.665 (0.573–0.737)	2.72	2.122	Default
Narrow n = 228)	410, 435, 460, 485, 560, 585, 610, 645, 680, 730, 760, 860, 900, 940 nm	SPAD	LR (4/5)	0.652 ± 0.033	0.591 (0.490–0.670)	3.005	2.302	Default
Wide, black (n = 140)	460, 730, 760 nm	SPAD	RF (2/5)	0.598 ± 0.067	0.534 (0.311–0.679)	4.909	3.575	Fold-specific
Wide, black (n = 140)	460, 485, 510 nm	%N	LR / KNN (2/5 each)	0.314 ± 0.079	0.202 (0.003–0.380)	0.616	0.442	Default / k = 7
Wide, black (n = 140)	510, 730 nm	Chl a (mg/g)	RF / KNN (2/5 each)	0.615 ± 0.028	0.604 (0.447–0.715)	0.789	0.612	Fold-specific
Wide, black (n = 140)	510, 535, 585, 610, 730, 760 nm	Chl b (mg/g)	KNN (4/5)	0.448 ± 0.050	0.395 (0.241–0.519)	0.735	0.573	k = 3–7
Wide, black (n = 140)	510, 730 nm	Total Chl (mg/g)	KNN (4/5)	0.594 ± 0.034	0.571 (0.408–0.692)	1.391	1.062	k = 3–7

performance is consistent with the pronounced optical sensitivity of chlorophyll within the visible and red-edge regions (Kushwaha et al., 2024), covered by the AS7265x. The specific spectral regions contributing to these predictions are discussed further in relation to wavelength selection.

Prediction performance and wavelength selection under wide and narrow measurement geometries

Prediction performance is summarized in Table 3, with complete OOF metrics in Supplementary Table S7. For SPAD, the full 18-channel models achieved OOF R^2 values of 0.665 in the narrow setup and 0.620 in the black wide setup, compared with 0.591 and 0.534 using RF-selected wavelengths, respectively. Here, ΔR^2 is defined as the R^2 for RF-selected wavelengths minus that for all 18 channels; a negative value favors the full-channel model. Paired bootstrap analysis gave $\Delta R^2 = -0.074$ (95% CI: −0.143 to −0.006) for narrow and −0.086 (95% CI: −0.160 to −0.024) for black wide (Table S8), supporting higher OOF R^2 with all 18 channels within both datasets. Under the white background setup, RF selection also yielded lower OOF R^2 for %N ($\Delta R^2 = -0.138$, 95% CI: −0.240 to −0.044) and chlorophyll a ($\Delta R^2 = -0.127$, 95% CI: −0.232 to −0.020). The remaining selected–full R^2 intervals included zero (Table S8).The confidence intervals describe uncertainty in each model's R^2 estimate but do not provide an inferential comparison of performance between the two geometries. Because the wide- and narrow-geometry experiments used independent samples collected in 2023 and 2026, respectively, and differed in other acquisition and preprocessing conditions, their numerical performance comparison is descriptive and cannot isolate the effect of measurement geometry.

The housing redesign altered both the nominal per-device field-of-view projection and the housing opening. The AS7265x consists of three spatially separated sensor devices, each with a built-in optical aperture of approximately 0.75 mm and a nominal field of view of ±20.5 (Sparkfun Electronics, 2023). Using the angular field of view about each device's optical axis $D = 2h\tan 20.5$, reducing the sensor-to-leaf distance from 110 to 10 mm decreased the calculated per-device footprint from approximately 82.3 to 7.5 mm. The housing opening was simultaneously reduced from approximately 80 to 30 mm. Previous AS7265x studies have primarily used housings to limit unwanted illumination, maintain sensor alignment, and stabilize the optical path (Lopin et al., 2025; Morales-Guerra et al., 2026; Sutherland et al., 2024). In the present study, the redesign additionally modified the sensor-to-leaf distance, nominal per-device footprint, and exposed opening area. For leaves 10–20 mm wide, a 7.5-mm footprint would be fully covered when the optical axis of each device was positioned over the leaf. However, because the three devices are spatially separated, the effective combined sampling area also

depends on device spacing and leaf alignment, which were not quantified. Assuming a straight, centrally positioned leaf spanning the 30-mm circular opening, 22–58% of the opening remained uncovered, as shown in Figure 1. This percentage represents exposed opening area rather than background directly contained within an individual device footprint. The footprint and opening reductions were intended to constrain direct leaf–background mixing and stray illumination, respectively, but their individual contributions to prediction error were not quantified. The remaining error may therefore reflect residual optical interference together with biological heterogeneity and reference-measurement variability.

The selected wavelengths generally corresponded to spectral regions previously associated with leaf pigment status. For SPAD, RF selection retained 2–9 channels across the five black wide-geometry outer folds and 13–16 channels across the narrow-geometry folds. The 460-, 730-, and 760-nm channels appeared in both experiments, although their selection frequencies differed (Fig. 5). The red-edge and near-infrared regions have previously been associated with rice-leaf SPAD (Yu et al., 2022). Because wavelength selection was repeated within each outer-training set, no single fixed subset generated all pooled OOF predictions.

For chlorophyll a, chlorophyll b, and total chlorophyll, 510 and 730 nm were selected in all five black-background outer folds, while additional wavelengths varied among folds. The selected subsets contained 2–5, 2–10, and 2–9 channels, respectively (Fig. 5). The 730-nm channel lies in the red-edge region and 510 nm in the green region, broadly consistent with reported chlorophyll-sensitive wavelengths (Guo et al., 2020; Huang et al., 2015). The broader selection pattern for Chl b may reflect overlap among the optical responses of chlorophyll a, chlorophyll b, and other leaf constituents (Zhang et al., 2019).

Chlorophyll b exhibited a more dispersed selection pattern than chlorophyll a, involving additional wavelengths in the blue, red, and near-infrared regions. This agrees with the reported sensitivity of chlorophyll b estimation to 630–660, 670–710, and 800–810 nm. The broader pattern may reflect spectral overlap between chlorophyll a, chlorophyll b, and other leaf constituents (Huang et al., 2015; H. Zhang et al., 2019). Although the final Chl b subset was also 510 and 730 nm, its fold-wise selection pattern was more dispersed than those of Chl a and total chlorophyll. This may reflect the substantial overlap between the optical responses of Chl a, Chl b, and other leaf constituents, which can make Chl b more difficult to resolve independently (H. Zhang et al., 2019).

In contrast, wavelength selection for leaf nitrogen was less stable across folds. The selected subsets contained 2–8 channels; 510 nm appeared in all five outer folds and 460 nm in four. These green and blue channels may provide indirect information about leaf %N through variation in chlorophyll and other pigments. In a recent leaf-level study of rice, green reflectance near 550 nm varied with nitrogen application, while leaf nitrogen concentration was associated with SPAD values (Zhang et al., 2024). More direct protein-related spectral information occurs in the short-wave infrared, including regions around 2060–2180 nm, beyond the 410–940 nm range of the AS7265x (Féretet al., 2021; Li et al., 2018). The absence of these protein-related bands may partly explain why leaf %N was predicted less accurately than the pigment-related traits.

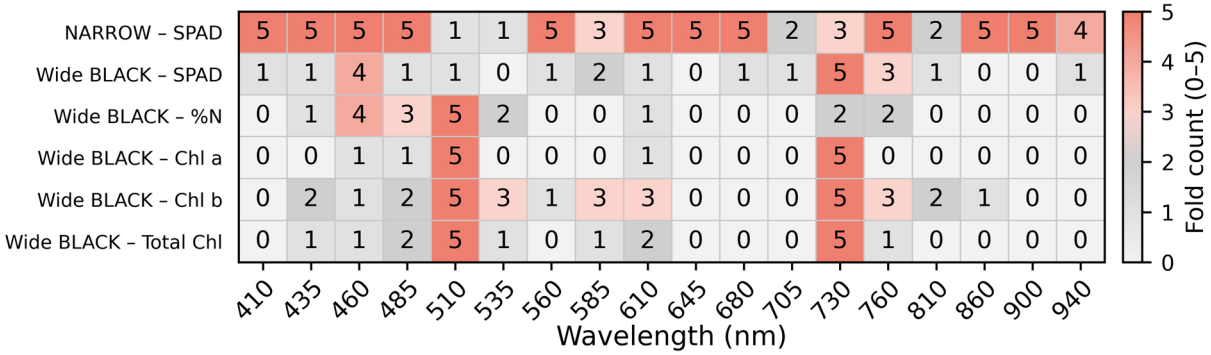

Figure 5. Wavelength-selection frequency across the five outer folds for RF-based feature selection. Rows represent SPAD under the narrow and wide geometries and %N, chlorophyll a, chlorophyll b, and total chlorophyll under the wide geometry. Higher counts indicate more stable wavelength selection across folds

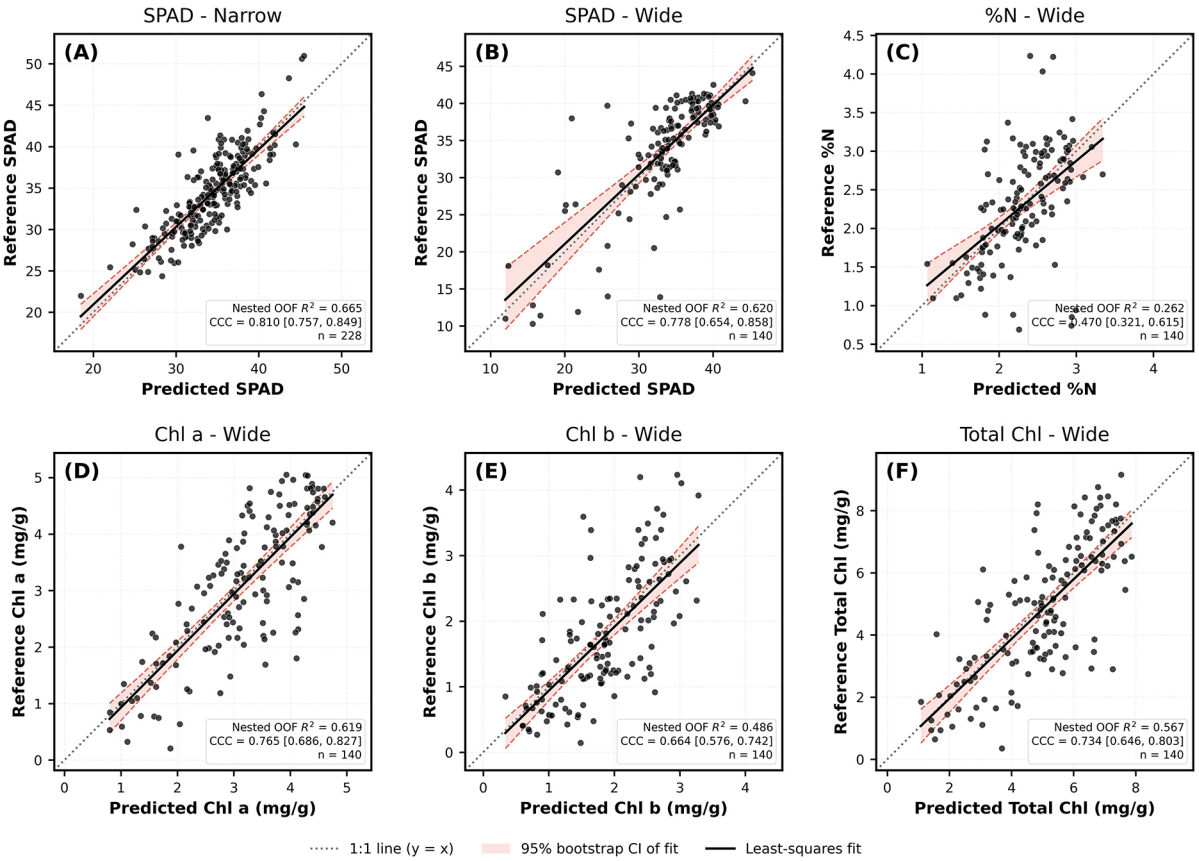

Figure 6. Agreement between reference values and nested out-of-fold predictions using all 18 wavelength channels. Panel (a) shows SPAD under the narrow geometry. Panels (b–f) show the wide geometry with a black background: (b) SPAD, (c) %N, (d) chlorophyll a, (e) chlorophyll b, and (f) total chlorophyll. Dotted lines indicate 1:1 agreement; solid lines show ordinary least-squares fits, and shaded bands show their 95% bootstrap confidence intervals. Corresponding results using RF-selected wavelength subsets are presented in Supplementary Figure S4

Agreement between nested OOF predictions and reference measurements

The narrow-geometry SPAD model showed the highest numerical agreement between nested OOF predictions and reference measurements (CCC = 0.810, 95% CI: 0.756–0.849; OOF R^2 = 0.665), followed by the full-channel black-background wide-geometry SPAD model (CCC = 0.778, 95% CI: 0.667–0.859; OOF R^2 = 0.620), as shown in Fig. 6a–f. The 95% CI spanned 0.093 for the narrow-geometry model and 0.192 for the wide-geometry model. This difference in interval width may partly reflect the larger sample size in the narrow experiment (n = 228 vs. n = 140). The corresponding RPIQ values were 2.340 and 1.737, respectively. Thus, relative to the interquartile spread of each reference dataset, the full-channel narrow model had a smaller OOF prediction error. The two geometries were evaluated using independently collected sample sets, so their numerical performance difference is descriptive and cannot be attributed solely to measurement geometry.

The CCC was used as a complementary measure of agreement rather than as a standalone indicator of predictive performance. It was originally proposed to evaluate reproducibility between repeated measurements and has subsequently been applied together with error-based metrics in environmental modelling and proximal soil sensing, including soil-property mapping for precision liming (Schmidinger et al., 2024)clay and pH. These maps can be generated with digital soil mapping models fitted on covariates observed by proximal soil sensors. However, the quality of the derived maps depends on the applied methodology. We assessed the effects of (i. However, CCC alone does not distinguish the relative contributions of correlation and bias, is sensitive to the variability of the evaluated data, and should not be compared directly across independent datasets with different distributions (Wadoux & Minasny, 2024)we illustrate

with synthetic examples three undesirable statistical properties of this coefficient. We argue that ignorance of these properties have led to a frequent misuse of this coefficient in modelling and mapping studies. The stand-alone use of the concordance correlation coefficient is insufficient because i. Accordingly, CCC was interpreted here together with nested OOF R^2, RMSE, and MAE and was decomposed into Pearson's correlation coefficient and the bias-correction factor Because nested OOF R^2 was calculated using the prediction-error formulation in Eq. (6), it also penalizes discrepancies between predicted and reference values. The additional contribution of CCC was therefore its decomposition into correlation and location–scale agreement.

Under the black-background wide geometry using all 18 channels, agreement was higher for chlorophyll a (CCC = 0.765), total chlorophyll (CCC = 0.734), and chlorophyll b (CCC = 0.664) than for leaf nitrogen (CCC = 0.470). For leaf nitrogen, the limited precision (= 0.523) was the primary contributor to the lower CCC, whereas the bias-correction factor = 0.900) indicated a smaller additional departure from perfect location–scale agreement. More specifically, the estimated scale ratio (= 0.627) together with the near-zero location shift (= 0.019) showed that the standard deviation of the predictions was approximately 63% of that of the reference measurements. The predictions were therefore compressed toward the reference mean rather than systematically shifted upward or downward. Although linear recalibration could potentially reduce this scale mismatch, it would not address the limited correlation; consequently, the improvement achievable through recalibration alone is likely to remain limited.

This distinction is relevant when sensor predictions are intended to support nutrient-management decisions because compressed or weakly correlated predictions may misclassify samples near nutrient-status thresholds. Nevertheless, agreement with reference measurements is a necessary but insufficient condition for fertilizer recommendation. Sensor-based nutrient-management studies have additionally validated sufficiency indices against observed crop responses, for example, aerial and proximal vegetation indices were evaluated against rice yield responses to top-dress N application across six site-years (Rehman et al., 2023). The %N model predicts laboratory-measured leaf nitrogen concentration under the study conditions, but its limited accuracy and the absence of validation against nitrogen-sufficiency thresholds or fertilizer responses preclude its use as a diagnosis of plant nitrogen status or a basis for fertilizer recommendations. The model has also not been externally validated on an independent rice sample set.

Study limitation

This study was limited to the IR64 rice variety and one general sampling area in Yogyakarta, which included several rice-field plots. The wide- and narrow-geometry experiments used different biological samples collected in 2023 and 2026, respectively. Differences in sampling year, reference-value distributions, and acquisition conditions therefore prevent the observed difference in SPAD prediction performance from being attributed specifically to measurement geometry. Model performance was estimated by nested cross-validation within each dataset; none of the models was externally validated on a separate sample set collected under additional conditions. Finally, the study did not assess whether the sensor estimates improve nitrogen-sufficiency classification, fertilizer application decisions, or crop responses to fertilization. These applications require dedicated validation before the system can be used for nutrient-management decisions.

CONCLUSIONS

Under the 2023 wide geometry, background configuration was associated with target-dependent differences in AS7265x prediction performance. In the 140 paired leaves, the full 18-channel models achieved higher OOF R^2 under black than white for chlorophyll a, chlorophyll b, and total chlorophyll, with 95% CIs for the paired differences excluding zero. The differences for SPAD and %N were inconclusive. White-background readings also showed higher raw signals, particularly in the blue region. These findings support monitoring and controlling the exposed background during spectral acquisition.

In the independent 2026 narrow-geometry dataset, the full 18-channel SPAD model achieved OOF R^2 = 0.665, RMSE = 2.720, MAE = 2.122, and CCC = 0.810. The black-background wide-geometry full-channel model achieved OOF R^2 = 0.620 and CCC = 0.778. This numerical difference cannot establish an advantage of the narrow geometry because the experiments differed

in year, biological samples, and other acquisition conditions. RF-based wavelength selection did not provide a supported improvement in R^2 over the full 18-channel scenario. For SPAD, the selected-wavelength models produced lower R^2 values in both the narrow-geometry and black-background wide-geometry datasets, while the wavelengths retained varied across folds and target traits. Prediction of leaf nitrogen was less accurate than that of the chlorophyll-related traits, with the black-background full-channel model yielding OOF $R^2 = 0.262$ and CCC = 0.470. Because this study involved IR64 rice from one general sampling area and lacked external validation, the findings require evaluation under additional conditions. The sensor outputs estimate measured leaf traits under the study conditions; independent validation on new rice samples and testing against nitrogen-sufficiency thresholds and fertilizer responses are required before their use for nitrogen diagnosis or fertilizer decisions.

Acknowledgements

We acknowledge the Indonesian Education Scholarship (BPI), the Center for Higher Education Funding and Assessment (PPAT), and the Indonesian Endowment Fund for Education (LPDP) for financial support for this research and graduate study under contract number 1398/J5.2.3/BPI.06/10/2021.

REFERENCES

1. Bellon-Maurel, V., Fernandez-Ahumada, E., Palagos, B., Roger, J. M., & McBratney, A. (2010). Critical review of chemometric indicators commonly used for assessing the quality of the prediction of soil attributes by NIR spectroscopy. *TrAC - Trends in Analytical Chemistry*, *29*(9), 1073–1081. https://doi.org/10.1016/j.trac.2010.05.006
2. Bi, S., Li, P., Lv, J., Dong, Q., Luo, X., Che, Y., Rehman, M., Liu, Z., Yu, C., & Peng, X. (2025). The optimized nitrogen rate reduced ammonia emissions from rice paddies in the cold region of Northeast China. *European Journal of Agronomy*, *164*(2024), 127444. https://doi.org/10.1016/j.eja.2024.127444
3. Carpenter, J., & Bithell, J. (2000). Bootstrap confidence intervals: when, which, what? A practical guide for medical statisticians. *Statistics in Medicine*, *19*(1999), 1141–1164. https://doi.org/10.1002/(sici)1097-0258(20000515)19:9<1141::aid-sim479>3.0.co;2-f
4. Chen, Y., Wang, X., Zhang, X., Xu, X., Huang, X., Wang, D., & Amin, A. (2024). Spectral-based estimation of chlorophyll content and determination of background interference mechanisms in low-coverage rice. *Computers and Electronics in Agriculture*, *226*(Sept.), 109442. https://doi.org/10.1016/j.compag.2024.109442
5. Féret, J.-B., Berger, K., Boissieu, F. de, & Malenovský, Z. (2021). Remote Sensing of Environment PROSPECT-PRO for estimating content of nitrogen-containing leaf proteins and other carbon-based constituents. *Remote Sensing of Environment*, *252*(112173). https://doi.org/10.1016/j.rse.2020.112173
6. Ghosh, M., Swain, D. K., Jha, M. K., Tewari, V. K., & Bohra, A. (2020). Optimizing chlorophyll meter (SPAD) reading to allow efficient nitrogen use in rice and wheat under rice-wheat cropping system in eastern India. *Plant Production Science*, *23*(3), 270–285. https://doi.org/10.1080/1343943X.2020.1717970
7. Girsang, S. S., Castillo, R. L., Syam, M., Zaini, Z., Kartaatmadja, S., Carla, J., Torre, D., Lorraine, I., Pabuayon, B., Hatta, M., Bagus, N., & Susanto, B. (2025). Field Crops Research Site-specific nutrient management for rice using soil properties to adjust phosphorus and potassium supply from compound NPK fertilizer. *Field Crops Research*, *326*(March), 109864. https://doi.org/10.1016/j.fcr.2025.109864
8. Govindasamy, P., Muthusamy, S. K., Tej, P., Jagannadham, K., Maity, A., Halli, H. M., Sujayananad, G. K., Vadivel, R., Das, T. K., Raj, R., Pooniya, V., Babu, S., Rathore, S. S., Muralikrishnan, L., & Tiwari, G. (2023). Nitrogen use efficiency—a key to enhance crop productivity under a changing climate. *Frontiers in Plant Science*, (3), 1–19. https://doi.org/10.3389/fpls.2023.1121073
9. Guo, W., Wang, K., Liu, Z., Zhang, Y., Xie, D., & Zhu, Z. (2020). Sensor-based in-situ detector for distinguishing between forchlorfenuron treated and untreated kiwifruit at multi-wavelengths. *Biosystems Engineering*, *190*, 97–106. https://doi.org/10.1016/j.biosystemseng.2019.11.019
10. Hale, G. A., Cox, R. D., & Ritchie, G. (2023). Canopy detection beyond the field: Colored backgrounds impact precision of Canopeo. *Sensing and Bio-Sensing Research*, *42*, 100587. https://doi.org/10.1016/j.sbsr.2023.100587
11. Huang, J., Wei, C., Zhang, Y., Blackburn, G. A., & Wang, X. (2015). *Meta-Analysis of the Detection of Plant Pigment Concentrations Using Hyperspectral Remotely Sensed Data*. 1–26. https://doi.org/10.1371/journal.pone.0137029
12. Kushwaha, A., Das, A., Dave, R., & Bhattacharya, B. K. (2024). A non-destructive estimation of chlorophyll-a and -b over different crops using airborne

imaging spectroscopy observations. *Advances in Space Research*, *73*(2), 1290–1303. https://doi.org/10.1016/j.asr.2022.07.060

13. Li, D., Wang, X., Zheng, H., Zhou, K., Yao, X., Tian, Y., Zhu, Y., Cao, W., & Cheng, T. (2018). Estimation of area- and mass-based leaf nitrogen contents of wheat and rice crops from water-removed spectra using continuous wavelet analysis. *Plant Methods*, *14*(1), 1–20. https://doi.org/10.1186/s13007-018-0344-1
14. Lichtenthaler, H. K., & Buschmann, C. (2001). Chlorophylls and carotenoids: measurement and characterization by UV-Vis spectroscopy. *Current Protocols in Food Analytical Chemistry*, *1*(1), F4.3.1-F4.3.8. https://doi.org/10.1002/0471142913.faf0403s01
15. Lin, L. I. (1989). A Concordance Correlation Coefficient to Evaluate Reproducibility. *Biometrics*, *45*(1), 255–268. https://doi.org/10.2307/2532051
16. Liu, L., Xie, Y., Zhu, B., & Song, K. (2024). Ecological Informatics Rice leaf chlorophyll content estimation with different crop coverages based on Sentinel-2. *Ecological Informatics*, *81*(May), 102622. https://doi.org/10.1016/j.ecoinf.2024.102622
17. Lizana, C. X., Pinochet, D., Sanda, P., & Soratto, P. (2025). *The nitrogen nutrition index as a tool to assess nitrogen use efficiency in potato genotypes*. *162*(Oct. 2024). https://doi.org/10.1016/j.eja.2024.127397
18. Lopin, P., Nawsang, P., Laywisadkul, S., & Lopin, K. V. (2025). Evaluation of Low-Cost Multi-Spectral Sensors for Measuring Chlorophyll Levels Across Diverse Leaf Types. *Sensors*, *25*(7), 1–26. https://doi.org/10.3390/s25072198
19. Mia, M. A. B., Das, M. R., Kamruzzaman, M., & Talukder, N. M. (2012). *Biochemical traits and physico-chemical attributes of aromatic-fine rice in relation to yield potential*. *2012*(12), 1788–1795. https://doi.org/10.4236/ajps.2012.312A219
20. Miao, X. X., Miao, Y., Liu, Y., Tao, S. H., Zheng, H. Bin, Wang, J. M., Wang, W. Q., & Tang, Q. Y. (2023). Measurement of nitrogen content in rice plant using near infrared spectroscopy combined with different PLS algorithms. *Spectrochimica Acta - Part A: Molecular and Biomolecular Spectroscopy*, *284*, 121733. https://doi.org/10.1016/j.saa.2022.121733
21. Morales-guerra, J., Soto-perdomo, J., & Botero-valencia, J. (2026). HardwareX Low-cost embedded system for spectral power distribution reconstruction for controlled environmental agriculture using a multispectral sensor and cloud-based deep learning. *HardwareX*, *26*(May), e00786. https://doi.org/10.1016/j.ohx.2026.e00786
22. Nogueira, F. H. M., dos Santos Teixeira, A., Ribeiro, S. G., Moreira, L. C. J., da Rocha Neto, O. C., Lopes, F. B., & Nogueira, R. E. F. Q. (2025). A Handheld Multispectral Device for Assessing Leaf Nitrogen Concentrations in Maize. *Sensors*, *25*(13), 1–18. https://doi.org/10.3390/s25133929
23. OSRAM, A. (2018). Product Document. In *ams OSRAM Group*. ams OSRAM Group. https://look.ams-osram.com/m/7ec5bcc3e40679be/original/TCS3472-DS000390.pdf
24. Pei, Z., Wu, X., Wu, X., Xiao, Y., Yu, P., Gao, Z., Wang, Q., & Guo, W. (2025). Segmenting vegetation from UAV images via spectral reconstruction in complex field environments. *Plant Phenomics*, *7*(1), 100021. https://doi.org/10.1016/j.plaphe.2025.100021
25. Rehman, T. H., Lundy, M. E., Reis, A. F. de B., Akbar, N., & Linquist, B. A. (2023). Reflectance Measurements from Aerial and Proximal Sensors Provide Similar Precision in Predicting the Rice Yield Response to Mid-Season N Applications. *Sensors*, *23*(13). https://doi.org/10.3390/s23136218
26. Sáez-Plaza, P., Navas, M. J., Wybraniec, S., Michałowski, T., & Asuero, A. G. (2013). An overview of the kjeldahl method of nitrogen determination. Part ii. Sample preparation, working scale, instrumental finish, and quality control. *Critical Reviews in Analytical Chemistry*, *43*(4), 224–272. https://doi.org/10.1080/10408347.2012.751787
27. Schmidinger, J., Schröter, I., Bönecke, E., Gebbers, R., Ruehlmann, J., Kramer, E., Mulder, V. L., Heuvelink, G. B. M., & Vogel, S. (2024). Effect of training sample size, sampling design and prediction model on soil mapping with proximal sensing data for precision liming. *Precision Agriculture*, *25*(3), 1529–1555. https://doi.org/10.1007/s11119-024-10122-3
28. Sparkfun Electronics. (2023). *(SparkFun Triad Spectroscopy Sensor - AS7265x (Qwiic) - SEN-15050 - SparkFun Electronics*. https://www.sparkfun.com/products/15050
29. Sutherland, C., Henderson, A. D., Giosio, D. R., Trotter, A. J., & Smith, G. G. (2024). HardwareX Synchronising an IMX219 image sensor and AS7265x spectral sensor to make a novel low-cost spectral camera. *HardwareX*, *19*(May), e00573. https://doi.org/10.1016/j.ohx.2024.e00573
30. Tian, B., Yu, H., Zhang, S., Wang, X., Yang, L., Li, J., Cui, W., Wang, Z., Lu, L., Lan, Y., & Zhao, J. (2024). Inversion of Cotton Soil and Plant Analytical Development Based on Unmanned Aerial Vehicle Multispectral Imagery and Mixed Pixel Decomposition. *Agriculture (Switzerland)*, *14*(9). https://doi.org/10.3390/agriculture14091452
31. Vijayaraghavareddy, P., Xinyou, Y., Struik, P. C., Makarla, U., & Sreeman, S. (2020). Responses of lowland, upland and aerobic rice genotypes to water limitation during different phases. *Rice Science*, *27*(4), 345–354. https://doi.org/10.1016/j.rsci.2020.05.009

32. Wadoux, A. M. J. C., & Minasny, B. (2024). Some limitations of the concordance correlation coefficient to characterise model accuracy. *Ecological Informatics*, *83*(September), 102820. https://doi.org/10.1016/j.ecoinf.2024.102820
33. Wang, Z., Tan, X., Ma, Y., Liu, T., He, L., Yang, F., Shu, C., Li, L., Fu, H., Li, B., Sun, Y., & Yang, Z. (2024). Combining canopy spectral reflectance and RGB images to estimate leaf chlorophyll content and grain yield in rice. *Computers and Electronics in Agriculture*, *221*, 108975. https://doi.org/10.1016/j.compag.2024.108975
34. Weng, X., Xu, H., & Jiang, D. (2005). *Characteristics of Gas Exchange , Chlorophyll Fluorescence and Expression of Key Enzymes in Photosynthesis During Leaf Senescence in Rice Plants*. *47*(5), 560–566. https://doi.org/10.1111/j.1744-7909.2005.00098.x
35. Xu, S., Xu, X., Blacker, C., Gaulton, R., Zhu, Q., Yang, M., Yang, G., Zhang, J., Yang, Y., Yang, M., Xue, H., Yang, X., & Chen, L. (2023). Estimation of leaf nitrogen content in rice using vegetation indices and feature variable optimization with information fusion of multiple-sensor images from UAV. *Remote Sensing*, *15*(12). https://doi.org/10.3390/rs15030854
36. Yang, B., Huang, X., Yan, X., Zhu, X., & Guo, W. (2020). A cost-effective on-site milk analyzer based on multispectral sensor. *Computers and Electronics in Agriculture*, *179*(August), 105823. https://doi.org/10.1016/j.compag.2020.105823
37. Yu, Z., Meng, L., Zhang, X., Liu, H., Han, Y., Lu, L., & Zhang, Z. (2022). *Improving SPAD spectral estimation accuracy of rice leaves by considering the effect of leaf water content*. (September), 2382–2395. https://doi.org/10.1002/csc2.20809
38. Yuan, Z., Cao, Q., Zhang, K., Ata-ul-karim, S. T., Tian, Y., & Zhu, Y. (2016). Optimal Leaf Positions for SPAD Meter Measurement in Rice. *Frontiers in Plant Science*, *7*(May), 1–10. https://doi.org/10.3389/fpls.2016.00719
39. Zhang, H., Duan, Z., Li, Y., Zhao, G., Zhu, S., Fu, W., Peng, T., Zhao, Q., Svanberg, S., & Hu, J. (2019). *Vis / NIR reflectance spectroscopy for hybrid rice variety identification and chlorophyll content evaluation for different nitrogen fertilizer levels*. *6*(191132). https://doi.org//10.1098/rsos.191132
40. Zhang, Y., Liang, K., Zhu, F., Zhong, X., Lu, Z., Chen, Y., Peng, Y., Pan, J., Lu, C., Huang, J., Ye, Q., Yin, Y., Mo, Z., & Fu, Y. (2024). Differential Study on Estimation Models for Indica Rice Leaf SPAD Value and Nitrogen Concentration Based on Hyperspectral Monitoring. *Remote Sensing*, *16*(23), 1–16. https://doi.org/10.3390/rs16234604